STRAIN-RATE DEPENDENT PROPERTIES OF CEMENT-BASED MATERIALS: A MULTI-SCALE EXPERIMENTAL AND MODELING EFFORT

Nathan P. Mayercsik[1], Cynthia Zingale Katcoff[2], Kimberly E. Kurtis[1], Lori Graham-Brady[2]

[1] School of Civil & Environmental Engineering, Georgia Institute of Technology
[2] Department of Civil Engineering, Johns Hopkins University

Introduction

OBJECTIVE: Quantify multiscale flaws/inclusions in cement-based material to better understand high strain-rate behavior of concrete

Blast or **impact loads** create a far-field compressive loading condition that drives local tensile crack growth from material flaws. Katcoff and Graham-Brady have created a model for high strain-rate compressive loading of brittle materials with **circular void flaws** following the model in [1] for **rectilinear flaws**. This 2D, flaw-driven, elastic model is used to predict material strength under a constant strain-rate loading with local stress intensity dictated by [2]. Here, **mortar** can be envisioned to contain flaws, such as pores and "slits" (or more linear defects such as interfaces) at various length scales. In order to develop a constitutive model for **high-strain rate behavior** of cementitious materials, this study presents a **multi-scale quantitative characterization** mortars with water-to-cement ratios (*w/c*) of 0.30, 0.40, and 0.50 with varying entrained air content (ϕ_2). The effect of flaws, including **macropores** (0.05–10 μm), **entrained air voids** (0.02 to 0.50 mm), and the **interfacial transition zone** (ITZ) around fine aggregates (0.15 to 0.59 mm nominal size), is considered (Fig. 1). Macropore networks are characterized via hydration simulations and x-ray microtomography. Mayercsik and Kurtis [3] have developed a probabilistic method to characterize entrained air voids in mortars using image analysis. The characteristics of the ITZ are to be studied by hydration simulations and compared with results obtained by nanoindentation. In future efforts, the high-strain rate compressive loading predictions of the micromechanics model will be verified with **Kolsky bar** tests.

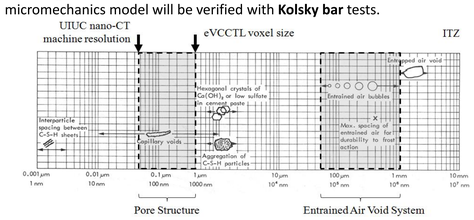

Figure 1: *Length scales of associated with flaws/ inclusion to be quantified* [4]

Micromechanics Model

For brittle materials, cracks initiate from existing material flaws. Paliwal and Ramesh [1] created a computational model using [2] and [5] to predict loss of material strength when cracks grow **rectilinear flaws** ("cracks") in a material. We expanded this work to create a **circular flaw** model. A model was created with the framework provided by [1].

Modeling Interaction

We assume a two-dimensional model. Flaw distribution is defined as the number of flaws per area. The model shown runs either a material with **rectilinear flaws** or **circular flaws**. From previous work, **it has been observed that cracks grow in the direction of the maximum compressive stress**. The model loading case is uniaxial compression.

The self-consistent method used by [1] considers each flaw individually as a single flaw **located within an ellipse of otherwise flawless material**. The local stress condition on the ellipse is computed from the global loading condition. Using stress intensity equations for a single flaw, we calculate the predicted crack growth caused by the local stress field. The area surrounding our flaw within an ellipse is seen as a matrix with effective weakened material properties. The weakening of this matrix depends on the summation of crack growth length from all the flaws in the material. Given material properties and loading condition, material strength depends on **number of flaws, flaw type**, and **flaw size**.

What the Model Does

- Computes crack growth from each flaw type and size
- Updates damaged properties of homogenized material
- Continues loading until post-peak/high damage

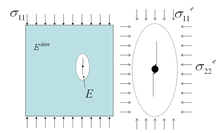

Figure 2: *Circular flaw model of Katcoff and Graham-Brady*

Pore Structure Characterization

We have identified **capillary pores** as the smallest voids that are likely to appreciably effect dynamic stress-strain response of cement-based materials. These voids range from about 10 nm to several microns in size (Fig. 1). Sampling for shapes, sizes, and spatial arrangements is difficult for tortuous networks that are not easily described by a particular geometry (e.g. "round," "elliptical," or "square"). Furthermore, the small scale requires high-resolution equipment and careful sample preparation to avoid artifacts. Some microstructural correlation functions must be probed from full 3D datasets, which rule out 2D microscopy. As such we have investigated two methods: **virtual hydration** and **x-ray microtomography** (x-μCT).

Data Collection

NIST's Virtual Cement & Concrete Testing Laboratory (**VCCTL**) can generate microstructures with a voxel size of **1 μm**. We collaborated with a group at the University of Illinois at Urbana-Champaign (UIUC) to obtain x-μCT data with voxel sizes approaching **500 nm** (Figs. 3,4).

Assessing Similarity

The standard **two-point correlation function**, $S_2(r)$, has long been understood to contain a host of important information regarding the properties of random media. The function gives the probability that both endpoints of a line of length r will lie in phase 2 (for this study, that is the porosity phase) [6]. However, reconstructions utilizing $S_2(r)$ alone have not proven to be entirely successful in all cases.

When paired with the **two-point cluster function**, $C_2(r)$, very good reconstructions have been obtained [7]. $C_2(r)$ is the probability that a line of length r lies entirely within the same cluster of phase 2 material [5].

We will determine if 3D images from VCCTL and x-μCT are **statistically similar** by :

1. Hydrating a virtual microstructure of hydrated cement paste (HCP)
2. Casting cement paste and analyzing via x-μCT
3. Calculating $S_2(r)$ and $C_2(r)$ from VCCTL and x-μCT
4. Comparing the sum of squares error between the two functions

Statistical similarity between the virtual (via VCCTL) and actual (via x-μCT) porespace will allow a host of factors to be observed by altering model inputs. Virtual hydration models are much **cheaper** and **faster** to obtain than x-μCT reconstructions.

Preliminary Results

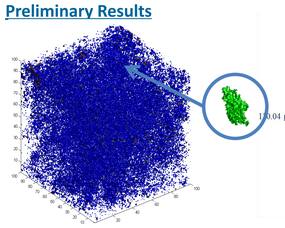

Figure 3: *Virtual microstructure (VCCTL)*

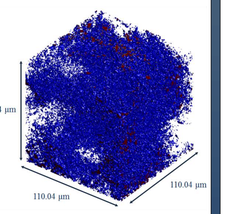

Figure 4: *Actual microstructure (x-μCT)*

Fig. 3 shows a 3D microstructure obtained by VCCTL (the green inset feature is the largest pore; the odd shape underscores the complex, non-Euclidean geometry of pore features). Fig. 4 shows a preliminary reconstruction of x-μCT slices from UIUC. The actual microstructure (Fig. 4) was cast from a standard reference cement purchased from NIST. The cement was chosen due to its chemical similarity to the cement in the hydration model. Fig. 5 shows the $C_2(r)$ for the virtual microstructure, showing the effect of varying the *w/c*.

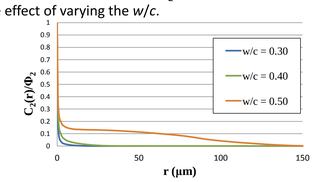

Figure 5: *Two-point cluster functions for cement 152 (VCCTL)*

Entrained Air Void Characterization

This research assumes the entrained air void system (a freeze/thaw durability requirement) to be a **polydispersed sphere system**. Utilizing work by Lu & Torquato [8], a robust probabilistic model for the spatial arrangement of the air void system may be obtained with the following data: the **volume fraction** of air voids, ϕ_2 (in the mortar phase), the **number density** air voids, ρ_v ,and the **first three moments** of the size distribution, $\langle R\rangle$, $\langle R^2\rangle$, $\langle R^3\rangle$.

While obtaining a volume fraction is rather straightforward with classical metallographic techniques, extracting a **three-dimensional size distribution** from **two-dimensional sections** is a challenging problem. We proceed as follows:

1. Obtain **digital images** from **plane, polished** concrete surfaces
2. Obtain the **lineal-path function** by analysis of digital images
3. Obtain the **size distribution** from the lineal-path function
4. Obtain ρ_v ,$\langle R\rangle$,$\langle R^2\rangle$, and $\langle R^3\rangle$ from the size distribution
5. Use data to calculate the **void "exclusion" probability**
6. Calculate the **mean nearest-surface distance**

Size Distribution

The **lineal-path function**, $L_i(z)$, is defined as the probability that a line of length z lies entirely within phase i [6]. It is related to the **chord-length probability density function**, $p_i(z)$, where $p_i(z)dz$ is the probability of finding a chord of length between z and $z + dz$ in phase i. For statistically homogenous isotropic media, the lineal-path function may be sampled from **plane cuts** [6]. Herein, it was obtained from binarized digital images using MATLAB scripts.

Figure 6: *Realizations of* $L_i(z)$ *and* $p_i(z)$

The lineal-path function may be probed from **two-dimensional images** and related to the **size distribution** by Eq. 1:

$$f(D) = \frac{2}{\pi\rho_v}\left(\frac{1}{z^2}\frac{d^2L_2(D)}{dD^2} - \frac{1}{z}\frac{d^3L_2(D)}{dD^3}\right) \qquad \textit{Eq. 1}$$

This significant contribution allows the size distribution to be expressed in **closed form** (differentiation was performed by finite difference). The value of ρ_v may be obtained from Eq. 1 by the definition of a probability density function (therefore $\int f(D)\, dD = 1$).

Spatial Arrangement

The **void nearest-surface probability density function**, $h_v(r)$, can describe the **spatial arrangement** of the voids statistically. $h_v(r)dr$ is the probability that at an arbitrary point in the system the nearest particle surface lies at a distance between r to $(r + dr)$ [8], as shown in Fig. 7. With the inputs discussed above (ϕ_2, ρ_v, $\langle R\rangle$, $\langle R^2\rangle$, and $\langle R^3\rangle$), a reasonable approximation may be obtained for the expression of $h_v(r)$ for three dimensional, polydispersed spheres.

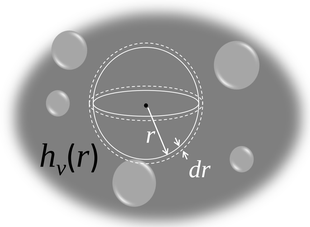

Figure 7: *Realizations of* $h_v(r)$

Entrained Air Void Characterization (con't)

Preliminary Results

From the expression of $h_v(r)$, we may obtain the mean **nearest-surface distance**, l_v , by $l_v = \int r h_v(r)\, dz$ [8]. We may obtain the variance as $\mathrm{Var}(r) = \int r^2 h_v(r)\, dz - l_v^2$ and standard deviation as $S = \mathrm{Var}(r)^{1/2}$. We define $\bar{M} = l_v + 3S$ and consider it a measure of a statistical maximum distance to the periphery of an air void from a point in the mortar. Fig. 8a shows $\bar{M}$ plotted against the ASTM spacing factor, $\bar{L}$. In the figure key, 'W,' 'S,' and 'V' denote wood rosin, synthetic, and Vinsol resin air entraining admixtures, respectively, and the numbers 41 or 45 denote w/c = 0.41 or 0.45, respectively. Closed data points reflect specimens that did not fail ASTM C666, while open data points failed. The data points are distributed much more evenly along the abscissa than the ordinate, where the failed points appear to cluster. This suggests that $\bar{M}$ is an **alternate descriptor** of failure. However, one data point (V45) has a very small and still fails ASTM C666. Fig. 8b shows that when plotted ρ_v is plotted against ϕ_2 , Vinsol resin samples tend to entrain fewer voids for a given air content, suggesting they create **coarser** entrained air void systems. Thus, **spacing alone does not fully explain freeze/thaw behavior**.

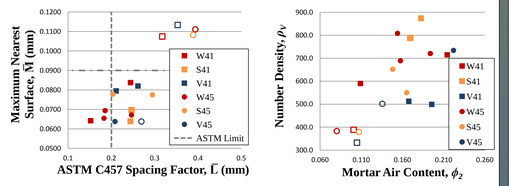

Figure 8: *(a) Comparison of spacing factors and (b) variation of number density versus mortar air content*

Interfacial Transition Zone Characterization

The ITZ is a rich source of flaws around aggregates, owing to the **elasticity mismatch** between the aggregate and hydrated cement paste, and the locally-higher volume fraction of **weak hydration products** and **porosity**. The co-PI's group has demonstrated the applicability of **nanoindentation** to quantity the length of the ITZ in ultra-high performance concrete [9], thereby providing information for the "slit" flaws (Fig. 9).

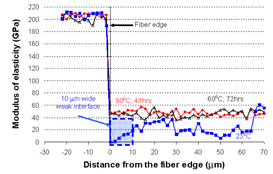

Figure 9: *Variation in paste modulus with distance from edge of a steel fiber*

In upcoming experiments, the ITZ will also be studied by observing the change in Young's modulus as a function of the distance from the edge of a fine aggregate particle. We employed VCCTL to design preliminary mixes and obtain estimated ITZ lengths (Table 1). Herein, ITZ length is considered to be the distance from the aggregate face at which the local Young's modulus reaches the global Young's modulus (Fig. 10).

Table 1: *Young's modulus and ITZ length from VCCTL simulations*

Sample	E (GPa)	ITZ (μm)
w/c = 0.3, ϕ_{air} = 0	29.64	10.5
w/c = 0.4, ϕ_{air} = 0	23.05	15.5
w/c = 0.4, ϕ_{air} = 0.10	23.07	20.5
w/c = 0.4, ϕ_{air} = 0.15	23.02	17.5
w/c = 0.5, ϕ_{air} = 0	18.20	19.5

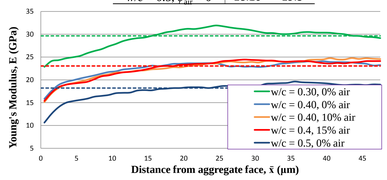

Figure 10: *Variation in paste modulus with distance from edge of fine aggregate. Dotted lines represent global values of E (results from VCCTL)*

Experimental Program

To evaluate the micromechanics models, five different mortar sample types will be cast which will **vary *w/c* and air content**. Samples will be cast at *w/c* = 0.3, 0.4, and 0.5 with no entrained air, and two additional samples will be cast at *w/c* = 0.4 with ϕ_2 = 0.10 and 0.15. The porosity is to be evaluated using mercury intrusion porosimetry, which will be compared to the host of data from VCCTL (see **Pore Structure Characterization**). Air entrained samples will be evaluated with the novel method presented herein. The ITZ around the fine aggregates will be measured by nanoindentation (see **Interfacial Transition Zone Characterization**).

High strain-rate experiments will be performed using a **Kolsky bar** (Fig. 11). The samples will be limited to cubes measuring 1 cm per side. Given the small sample size, only three size classes of fine aggregates will be used: those retained on No. 30, No. 50, and No. 100 sieves. The proportions of each will be scaled from a fine aggregate which passes ASTM C33 gradation limits (Fig. 12) to cast a representative mortar. The sand-cement-water ratio will be based on ASTM C109.

Figure 11 *Kolsky bar apparatus*

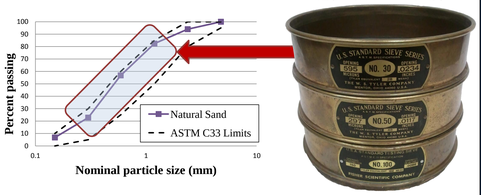

Figure 12: *Sieve analysis for experimental program*

Conclusions

- A new micromechanics model has been developed **to incorporate circular flaws**, enabling inclusions to be modeled as either circular flaws or rectilinear slits
- Techniques have been developed to assess porosity, entrained air voids, and ITZ. These techniques have far-reaching applicability **outside the realm of dynamic behavior** of cement-based materials
- **An experimental plan** has been designed to assess the effects of a host of controlled flaws on high strain-rate behavior of mortar

Acknowledgement

This material is based upon work supported by the National Science Foundation under Grant No. CMMI-0970049. Any opinions, findings, and conclusions or recommendations expressed in this material are those of the authors and do not necessarily reflect views of the National Science Foundation.

References

1. B. Paliwal, K.T. Ramesh, "An interacting micro-crack damage model for failure of brittle materials under compression," *Journal of Mechanics and Physics of Solids*, vol. 56, no. 3, pp. 896-923, 2007.
2. C. G. Sammis, M. F. Ashby. "The failure of brittle porous solids under compressive stress states," *Acta Metallurgica*, vol. 34, no. 3, pp. 511-526 (1986).
3. N.P. Mayercsik, K.E. Kurtis. "A probabilistic image-analysis technique for entrained air void analysis in hardened concrete," manuscript.
4. P.K. Mehta, P.J.M. Monteiro, Concrete: microstructure, properties, and materials, third edition, New York: McGraw Hill, 2006.
5. M. F. Ashby, S. D. Hallam. "The failure of brittle solids containg small cracks under compressive stress states," *Acta Metallurgica*, vol. 34, no. 3, pp. 497-510 (1986).
6. S. Torquato, Random Heterogeneous Materials: Microstructure and Macroscopic Properties., New York: Springer-Verlag, 2002.
7. Y. Jiao, S. Torquato, F. Stillinger,"A superior descriptor of random textures and its predictive capacity," in *Proceedings of the National Academy of Science*, 2009.
8. B. Lu, S. Torquato, "Nearest-surface distribution functions for polydispersed particle systems," *Physical Review A*, vol. 45, no. 8, pp. 5530-5544, 1992.
9. V.Y. Garas, K.E. Kurtis, L.F. Kahn, "Creep of UHPC in tension and compression: Effect of thermal treatment," *Cement and Concrete Composites*, vol. 34, no. 4, pp. 493-502, 2012.